Article

High-Fidelity Modeling and Investigation on Blade Shape and Twist Angle Effects on the Efficiency of Small-Scale Wind Turbines

Widad Yossri [1], Samah Ben Ayed [2] and Abdessattar Abdelkefi [1,*]

[1] Department of Mechanical and Aerospace Engineering, New Mexico State University, Las Cruces, NM 88003, USA
[2] Department of Engineering Technology and Surveying Engineering, New Mexico State University, Las Cruces, NM 88003, USA
* Correspondence: abdu@nmsu.edu

Abstract: A high-fidelity analysis is carried out in order to evaluate the effects of blade shape, airfoil cross-section. as well as twist angle distribution on the yielded torque and generated power of a horizontal axis Small-Scale Wind Turbine (SSWT). A computational modeling and an effective design for a small turbine with a blade length of 25 cm subject to a 4 m/s freestream velocity are presented, in which a segregated RANS solver is utilized. Four airfoil profiles are assessed, namely NACA0012, NACA0015, NACA4412, and NACA4415, and two blade shape configurations, rectangular and tapered, are evaluated. The flow around the rotating turbines is investigated along with blade stresses and performance output for each configuration. Subsequently, the impact of various linear and nonlinear twist distributions on SSWT efficiency is also examined. Results show that for the studied operating conditions corresponding to low-speed flows, the rectangular blade configuration outperforms the tapered blade shape from the generated torque and power perspectives, while the tapered shape configuration represents an attractive design choice from the yielded stresses point of view. Additionally, while the nonlinear twist configuration results in the best performance among the configurations studied, an SSWT blade design implementing a linear twist distribution can be highly competitive provided that a good slope is carefully selected.

Keywords: small-scale horizontal axis wind turbines; high-fidelity simulations; flow visualization; blade geometry; twist angle; energy efficiency

1. Introduction

In view of the swift evolution of global warming, the topic of renewable energies as potentially efficient substitutes for fossil fuels has reached the forefront of the scholarly community's focus. Wind turbines represent harvesters that are able to convert wind energy into mechanical energy by virtue of the rotation of the blade, eventually converting the generated mechanical energy into electrical energy through the generator [1]. Every single wind turbine is a complex system comprising various components. Wind turbine blades, in particular, are critical components of the wind turbine since they are responsible for harnessing the wind potential and driving the rotation of the rotor [2]. Therefore, efforts ought to be concentrated on the effective design of the aerodynamics of wind turbine blades.

Generally, many investigations of the aerodynamics governing the functioning of turbine blades are carried out under the long and slender structure assumptions [3], in which turbine blades are considered to be slender structures, where the velocity in the spanwise direction is considerably lower than in its counterpart component in the streamwise direction [3]. Under these specific circumstances, it is acceptable in many research efforts that the flow at a specific radial position is two dimensional, where 2D airfoil analyses can be both practical and accurate, specifically for conditions characterized by low wind speed [4–6].

However, additional intricacies should be considered when dealing with small-scale wind turbines: First, the low aspect ratio characterizing small-scale wind turbines stresses the importance of revisiting the assumptions of the infinite wing valid only for the specific case of very long blades [7–9]; second, the apparent differences in operating environments between horizontal axis large-scale wind turbines (LSWTs) and their small-scale counterparts, namely speed of the freestream wind, air turbulence, Reynolds number, etc. accentuates the necessity of analyzing the aforementioned turbines depending on their specific operating conditions. In view of the exponential growth of wind speed as a function of height [10], the functioning of the LSWT is characterized by speeds higher than those undergone by the SSWT, since the latter usually reach heights approximately fourteen times lower than their large-scale equivalents [11]. Being mounted at lower altitudes, SSWTs face more turbulent winds as a result of the presence of numerous obstacles within the same height range, namely trees and buildings [12–15].

In light of all the aforementioned differences, it is of great importance to assess the performance of each of the small- and large-scale wind turbines while considering each turbine's own proper set of operating conditions, as failing to do so might lead to deceptive outcomes and wasted efforts. It is indisputable that during recent decades, the wind energy sector has witnessed numerous advancements, especially when it comes to the industrial scale. Nevertheless, a larger room for contribution is still available from the small-scale, as the peer-reviewed literature and investigative studies dedicated to SSWTs are, by comparison, far smaller than that available for LSWTs, despite their considerable energy potential [16].

The overall design of a wind turbine unfolds under numerous considerations, one of which is blade shape. The main objective of the optimization of a wind turbine's blade shape is to attain maximized torque and minimized thrust. For that, turbulence is an important criterion to explore. It can be more pronounced either by a roughening in the body surface or a sharp edge on the body [17]. Investigation of the blade's interactions with the wind, including turbulence, is a necessary step in the aerodynamic optimization process. The power and noise produced by the turbine depend on the turbulence over the blade. Added turbulence will change the pressure profile around the airfoil and, consequently, the aerodynamic forces. In the case of a flat plate, a separation of the boundary layer is created at the sharp edges, making the drag coefficient at that specific point significantly less dependent on the Reynolds number (Re) and largely more dependent on the plate's aspect ratio (AR). A taper in the blades is therefore introduced in order to gently minimize the pressure gradient at the tip portion of the blade, which helps produce a narrower wake as well as very low drag [18]. Another crucial design parameter of a wind turbine blade is the twist angle. The optimal angle of attack of the airfoiled cross-section of the blade is heavily affected by the faced wind direction. Alternatively, apparent wind direction is affected by the speed of the rotating blades, even in uniform freestream wind velocity conditions. To achieve a certain rotations-per-minute rate, the tip cross-section of the blade always travels faster than the cross-section located near the rotor hub. In other words, as the wind turbine blade rotates, the tip of the blade must travel a bigger distance than the section of the blade closer to the hub in order to maintain the same rotational speed. This means that the tip of the blade must travel more quickly than the section of the blade closer to the hub in order to maintain the same rotational speed. Therefore, it seems only logical that the different cross-sections along the blade are not going to have the same optimal angle of attack. To this end, optimized designs of wind turbine blades have adopted a varying twist throughout the length of the blade in order to achieve an optimal angle of attack along the entirety of the length.

In order to address the above-mentioned crucial design parameters, numerous research efforts were dedicated to exploring several blade shapes and twist angle configurations, with the shared objective of achieving an aerodynamically efficient design for a wind turbine to reach the maximum attainable power adequate for a selected set of environmental operating conditions. For instance, a study by Rahgozar et al. [19] assessed the performance

of a small horizontal axis wind turbine with regard to the output power and the starting time for four different combinations of linear/nonlinear distributions of the chord length and twist angle along one-meter timber blades. The results of this study show that, even though the linear distributions deviate more from the ideal distributions compared to the nonlinear distributions, they still perform similarly in terms of generating power output. Xudong et al. [20] aimed at optimizing the blade shape for 2 MW and 5 MW turbine rotors. Their effort was based on the blade element momentum (BEM) theory with a refined tip-loss correction; their work showed that the optimization model indeed reduced the energy cost in the case of the studied rotors. Tenguria et al. [21] also used the BEM theory to identify the best combination of multiple design parameters, namely the chord, thickness, and twist distribution, basing the blade's cross-section on two selected NACA airfoil profiles. The BEM method was also the foundation of a research effort by Tahani et al. [22], where the goal was obtaining the maximum power coefficient for linearized chord and twist distributions. Similarly, The BEM theory was used in various studies dedicated to improving LSWT designs [23–28]. On the other hand, the latter theory was also relied on in several small-scale optimization studies. Tahani et al. [29] created an optimization code for the SSWT case and provided validation of the experimental data for a specific case of operating conditions. Additionally, Chaudhary et al. [30] conducted a study in which the BEM theory was utilized in order to optimize the blades' number and the selection of tip speed ratio. The BEM method was also utilized in a research effort by Tahani et al. [31]. The aim of this research study was proposing a new approach to introducing chord and twist distributions through fitting various types of functions on them. To this end, 48 functions were chosen, based on their resemblance to the classical distributions, as potential distributions for chord and twist angle profiles. Several functions were proposed, with the aim of maximizing the power coefficient. In other efforts led by Pourrajabian et al. [32,33], the objective was to design a fast-starting blade where the starting time was combined with the output power towards an objective function, while the blade's tolerable stress was considered as the system's constraint value and the BEM theory was considered the basis of the optimization code, as was the case for numerous other studies dedicated to improving the performance of SSWTs [34–38], some of which were very recently published.

The BEM theory is not exempted from a set of assumptions that make it unable to provide real-time intricate information that may be important; for instance, a lack of accuracy in flow representation due to a disregard for wake expansion and tip losses, which can have significant effects, especially in fluid–structure interaction analyses. In fact, many research efforts have attempted to solve this issue by providing several corrections to the original theory [39–42]. Additionally, the BEM theory necessitates non-turbulent air movement for the equations to be calculated. This is problematic since, in the case of the SSWTs especially, the flow is characterized by a high turbulence induced by same-height-range obstacles, as discussed previously. This means that relying on the BEM for analysis of SSWTs will most likely generate best-case idealistic scenarios instead of realistic pictures of performance. Moreover, SSWT blades are characterized by smaller aspect ratios compared to their large-scale counterparts. For this scenario, neglecting 3D flow effects is more consequential, which makes the BEM theory more inadequate for SSWT analyses since it is based on calculating the aerodynamic forces acting on every cross-section along the blade while assuming the latter to be two-dimensional [43].

Hence, high-fidelity analyses able to fully capture the 3D flow behavior around the three-dimensional rotating turbine are necessary, especially when investigating the efficiency of SSWTs. Several computational fluid dynamics (CFD) studies were carried out to assess industrial-scale wind turbines, leading to highly efficient designs [44–50], while not as many peer-reviewed resources are available for their small-scale equivalents [51–54]. Additionally, the literature regarding the shape of the blade and the twist distribution specific to SSWTs still has major room for contribution.

The purpose of this study is to use a high-fidelity CFD approach to examine the effect of blade shape and twist angle on the power output of a 50 cm rotor diameter wind

turbine. The analyses include a comparison of rectangular and tapered blade shapes using four airfoils with high lift-to-drag ratios via solving the full Navier–Stokes equations. Additionally, different twist configurations are evaluated, and the optimal design is selected based on torque and power computations. The numerical simulations are conducted using COMSOL Multiphysics, a finite element (FE)-based software.

2. Modeling and Numerical Implementation

### 2.1. SSWT Geometric Modeling Considerations

The utilized 3D turbine models are developed using SOLIDWORKS and then imported to COMSOL Multiphysics. The analyses carried out in this research effort mainly focus on the effects of blade shape in conjunction with airfoil selection on turbine efficiency from the generated torque and produced power perspectives, in addition to investigating the twist distribution effect on the aforementioned performance/efficiency indices. To this end, a total of eight different turbine geometries are assessed in the first part of the study, where the four airfoils, namely NACA0012, NACA0015, NACA4412, and NACA4415, are investigated for the rectangular blade shape and the tapered blade shape individually while a similar twist distribution is maintained. The most effective cross-sectional airfoil configuration is then carried out in the second part of the study to evaluate the effect of the twist distribution on the performance of SSWTs. Seven additional blade geometries are developed, each with a specific twist distribution characterized by different linear/nonlinear distributions and slope characteristics using the effective airfoil from the previous study. The flow behavior, stresses, as well as performance of each are independently assessed. The aim is to evaluate the impact of each design characteristic on the overall performance of the SSWT and come up with the most effective combination of the latter parameters that ensures ease of manufacturing with the least efficiency compromise.

During the CAD development and design stages, two important points are considered: the geometry simplification and the rigor of comparison. First, the developed 3D geometries should be simplified for the ease of the meshing process while not being too oversimplified, which might lead to failure in portraying the true aerodynamic characteristics. To this end, the hub attachment is represented with a cylindrical connection since it has minimal influence on the aerodynamic performance of SSWTs, whereas the blades, being the most aerodynamically important constituents, are not subject to any oversimplifications. Second, a comparison of various blade shapes is developed for designs that undergo similar flow conditions: a similar Reynolds number of approximately $R_e = 2 \times 10^4$ as well as a turbine blade surface area of $A_{blade} = 2.4 \times 10^{-2}$ m² are maintained. Indeed, the value of the constant chord length in the rectangular blade configurations is set to the average chord length value of the tapered blade configurations, for which the tapering varies linearly from the root to the tip. This simultaneously ensures that the overall surface areas of the studied SSWT designs are the same while guaranteeing that the average Reynolds number characterizing the flow is constant regardless of the considered turbine design. Table 1 shows the geometric properties of the rectangular and tapered blades studied, and Figure 1 illustrates the developed rectangular and tapered CAD models for the example of the NACA4412 airfoil.

The second part of the analysis evaluates the effect of the twist distribution on the SSWT power generation. For this purpose, a total of seven twist distributions are studied. The aim is to evaluate different linear and nonlinear configurations of the twist angle distributions and to assess the influence of the nonlinearity as well as the slope steepness on the performance of SSWTs operating in low-speed conditions. Figure 2 shows an example of the developed designs for the case of the tapered blade shape with linear and nonlinear twist distributions.

Table 1. SSWT design characteristics.

| Characteristic	Design Configuration	
	Tapered	**Rectangular**
Hub chord	6.1×10^{-2} m	4.3×10^{-2} m
Tip chord	2.5×10^{-2} m	4.3×10^{-2} m
Single blade overall surface area	2.4×10^{-2} m^2	2.4×10^{-2} m^2
Tip speed ratio (λ)	1.3	1.3
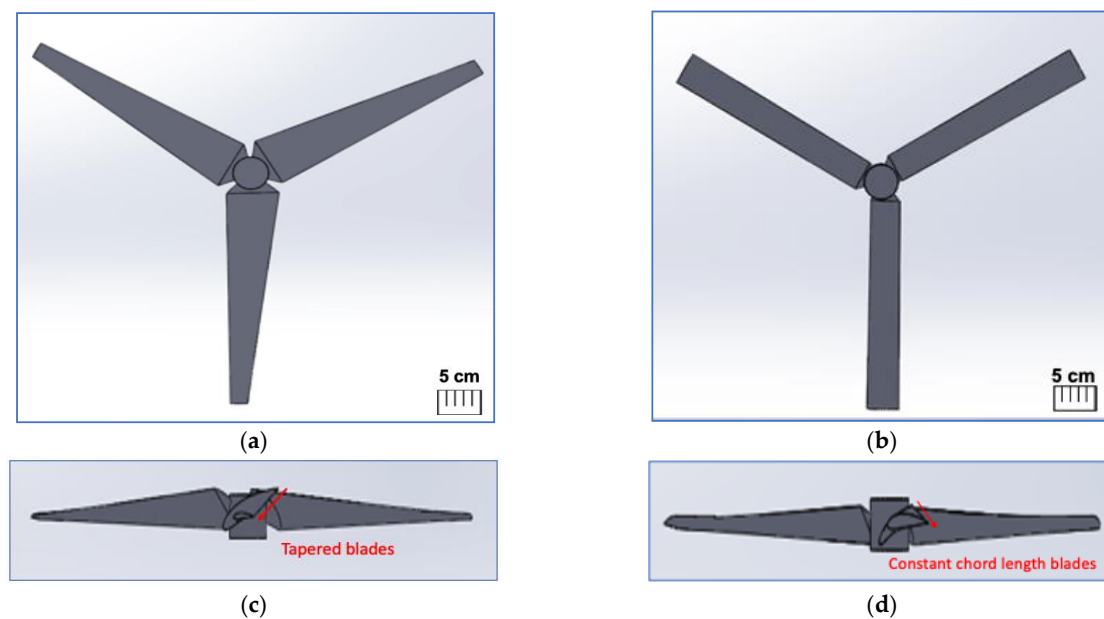
Figure 1. SSWT CAD designs with (**a**,**c**) tapered and (**b**,**d**) rectangular configurations for the NACA4412 airfoil, with x-z view (**top**) and y-x view (**bottom**).

An effective nonlinear distribution developed using the BEM theory [16] is used as a starting configuration (Fit A). A linear design configuration is also developed maintaining the same twist at the hub and tip. Thereafter, in order to assess the slope effect, two additional SSWT CAD models are designed with linear and nonlinear configurations, with different slopes and steepness levels, as shown in Figure 3. Moreover, an additional model with a linear twist distribution (Fit G) is created. The aforementioned distribution is obtained by linearizing the mid-nonlinear case; however, instead of the previous approach of maintaining the same twist at the hub and tip, another approach of least-square linearization is adopted. In other words, a linear twist configuration is generated by minimizing the sum of the squares S of the residuals r_i, which are simply the differences between the nonlinear distribution and the fitted linear one at each point along the blade, as follows:

$$r_i = y_i - \hat{y}_i \tag{1}$$

$$S = \sum_{i=1}^{n} r_i{}^2 = \sum_{i=1}^{n} (y_i - \hat{y}_i)^2 \tag{2}$$

where y_i is the data from the effective nonlinear twist configuration, $\hat{y}_i$ denotes the generated linear fit point, and n represents the number of the considered data points included in the fit. The purpose of this particular study is to evaluate the potential of linear twist configurations, since they are more attractive due to ease of manufacturing, and to assess their competitiveness when compared to nonlinear distributions in the case of low-speed operating SSWTs. Table 2 sums up the characteristics of the seven twist distributions used.
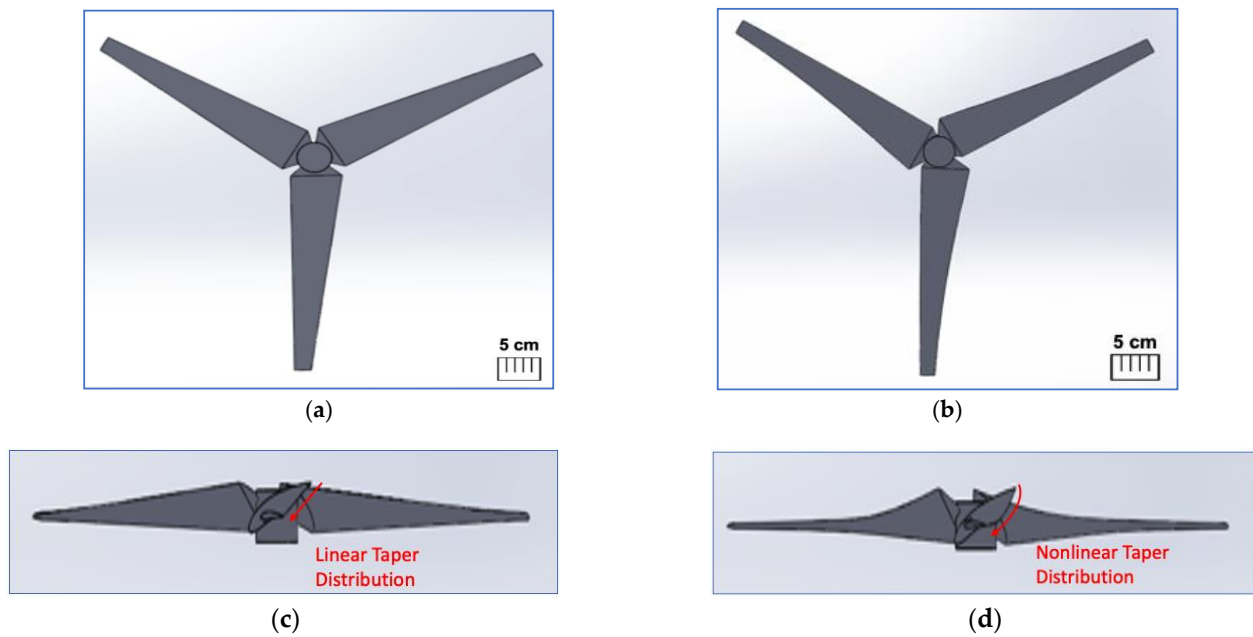
Figure 2. SSWT CAD designs with (**a**,**c**) linear and (**b**,**d**) nonlinear twist distributions for the NACA4412 airfoil, with x-z view (**top**) and y-x view (**bottom**).
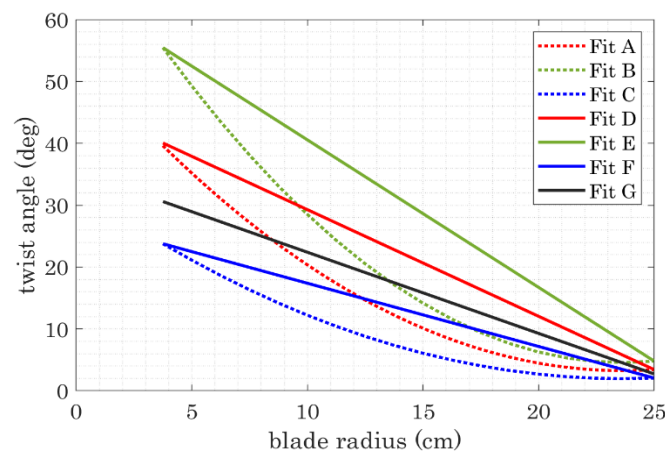
Figure 3. SSWT CAD design twist angle distributions.

Table 2. Twist distributions.

Twist Distribution	Type	Descriptive Equation	Slope (for Linear)	Slope Magnitude Percent Increase/Decrease (with Regards to fit D)
Fit A	Nonlinear	$0.09\,r^2 - 4.35\,r + 54.61$	-	-
Fit B	Nonlinear	$0.13\,r^2 - 6.08\,r + 76.46$	-	-
Fit C	Nonlinear	$0.06\,r^2 - 2.61\,r + 32.77$	-	-
Fit D	Linear	$-1.72\,r + 46.51$	-1.72	0%
Fit E	Linear	$-2.38\,r + 64.39$	-2.38	40% steeper
Fit F	Linear	$-1.02\,r + 27.59$	-1.02	40% less steep
Fit G	Linear	$-1.30\,r + 35.33$	-1.30	24% less steep

2.2. Flow Modeling Accuracy and Convergence Considerations

The overall characteristics of the fluid motion across the turbine are solved using 3D Navier–Stokes equations. The equations are solved using COMSOL Multiphysics. The flow is governed by the momentum balances and the continuity equations, forming four main coupled equations in 3D, and are, respectively, represented in a general form as:

$$\rho \frac{D\vec{\mathbf{u}}}{Dt} = -\nabla p + \rho \vec{g} + \mu \nabla^2 \vec{\mathbf{u}} \tag{3}$$

$$\nabla . \vec{u} = 0 \tag{4}$$

where μ denotes the dynamic viscosity, ρ the density of the fluid, and p represents the pressure.

Accurate fluid representation and modeling is a vital step, especially in flow governed analyses. One of the main important flow characteristics, especially in 3D modeling, is turbulence. In fact, a correct turbulent modeling accurately captures 3D flow tendencies, and therefore provides accurate insights about potential losses induced by flow behavior. Low Reynolds number flow analyses are an even greater challenge in the selection of the most appropriate turbulence model. In fact, associating low Reynolds number flows with turbulence modeling almost appears to be opposing in view of the fact that, classically, a low Reynolds number is the key characteristic of a laminar flow, and that the flow can only be described as turbulent if the associated Reynolds number is high. However, in the specific of case of airfoils subject to low *Re* numbers, resistance to the boundary layer's induced separation is very weak. This leads to a dominant adverse gradient of the pressure around the airfoil. Therefore, due to the rise in the adverse pressure at the leading edge, the flow separation phenomenon occurs and the separated flow is extremely unstable. As a consequence, a transition zone immediately forms downstream, leading the flow to become more turbulent [55]. Therefore, low *Re* number turbulence models are necessary to correctly reproduce the behavior of the fluid flow as the distance to the wall approaches zero, which leads to a more robust boundary layer flow solution [56].

In the presented study, the k-ε turbulence model is selected thanks to its capability of correctly modeling flows around complex geometries and its ease of convergence. As a tradeoff, very fine mesh elements are used near the turbine wall in order to ensure a correct flow solution near the rotating geometry, and a convergence analysis, the details of which will be discussed later, is performed to ensure that the number of mesh elements is sufficient to accurately model the flow in the entirety of the computational domain. The "Wall Function Interface" feature in COMSOL is utilized to automatically set the y+ value based on the chosen turbulence model and wall function, while a y+ threshold of five is maintained. In addition, since convergence may be a challenge for complex flow simulations, ensuring that solid initial guesses are passed to the solver is important. If a good estimation is known based on a preliminary analytical solution of a simplified version of the problem, it can be entered as an initial value. Nevertheless, since the problem in hand deals with complex flows and intricate 3D geometry, good initial guesses are obtained through a *Frozen Rotor* stationary study that is resolved prior to the time-dependent study to guarantee that good initial guesses are supplied to the solver as a strong foundation for the iterative approach that computes the flow around the rotating geometry subject to a 200 rpm rotational rate.

Another important aspect for convergence is satisfying the Courant–Friedrichs–Lewy (CFL) condition, especially for the numerical solution of certain partial differential equations. This is done by carefully selecting the time step so that, for each iterative step, the CFL value is less than its tolerated maximum CFL_{max}. In this study, the flow solutions to the presented models are obtained using an adaptive time stepping. This ensures that an optimal CFL number is attained by performing automatic adjustments to the selected time step during every iteration, in order to speed up the simulation while maintaining a high stability. Therefore, rather than a constant time step, the current simulations are

characterized by iterative conditional time stepping, where the maximum limit of the time step was manually set to 0.05 s.

The solver type is also adjusted for the flow analysis, where a combination of the direct and iterative solvers is used. In this study, Parallel Sparse Direct Solver (PARDISO) is used for the direct solution of the linear system of equations. This solver type is mainly used for simulation types that require memory efficiency and high performance due to the large sparse symmetric and nonsymmetric systems of equations to be solved. For the iterative approach, the restarted generalized minimum residual (GMRES) method is used. It is an iterative approach used to solve linear systems; its strength is fast convergence on condition that appropriate preconditioner and initial conditions are provided [57]. In this study, this prerequisite is satisfied through the use of a dual-step study approach, where the solution of the first stationary study is used to provide solid initial guesses to the time-dependent rotating rotor analysis, as said previously.

The finite element discretization scheme generates an implicit ODE system that is solved with predefined accuracy through relative and absolute tolerances. These are assigned requirements for the time-stepping solver and algebraic solver, respectively. The relative tolerance (Rtol) represents a set value that is used in each iteration and is assigned to all the dependent variables. Its value ranges between 0 and 1 and is a dimensionless quantity; a small value of the aforementioned parameters results in smaller time steps, which automatically increases the solution's accuracy at the cost of an extensive computational time. On the other hand, contrary to the relative tolerance, the absolute tolerance (Atol) is assumed to hold the same units as the dependent variables to which it applies, and can be a global value or an individual set of values independently applied to each dependent variable. For this study, the value of the latter parameter is calibrated for fluid flow simulations. Table 3 encapsulates all the solver details for this study. It should be mentioned that the rotor–stator coupling interface was addressed via the *Form Assembly* feature in COMSOL Multiphysics, where identical superposed cylinders were created and *identity pairs* were created in between.

Table 3. 3D solver options.

Criterion	Type
Study Step 1	Frozen rotor (Solid initial guesses provider)
Study Step 2	Time dependent (Transient solution provider)
Direct solver	Parallel Sparse Direct Solver (PARDISO)
Algebraic multigrid solver	Generalized minimum residual (GMRES)
Relative tolerance (Rtol)	0.001
Absolute tolerance (Atol)	Calibrated for fluid flow analyses
Time step (Δt)	Adaptive time stepping (CFL condition)
Turbulence model	Low *Re* k-ε model associated with a mesh refinement at the wall
Flow type	Incompressible
Solution time	15 s
Average computational time	~5 days
Running setup	Intel® Core™ i7-8700B Processor (12 M Cache, up to 4.60 GHz)

2.3. Computational Domain and Meshing Considerations

The constructed computational domain is composed of two regions: an outside rectangular region with relatively coarser stationary mesh; and an inside cylindrical moving mesh, with finer elements as the distance towards the rotating turbine decreases. A boundary layer mesh is constructed near the turbine surface to better capture the flow details near the rotating turbine boundary, and free tetrahedra are used as meshing elements for the

remainder of the computational domain. In analyses studying the flow behavior around a rotating geometry or turbomachinery, the integration of a moving mesh is paramount to best mimic the motion of the rotating structure. To this end, the cylindrical moving region is translationally fixed and rotates around the designated rotational axis, as does the turbine. Since this aforementioned region is characterized by denser mesh, the larger its volume within the whole computational domain, the larger the number of elements of the entire mesh, and, consequently, the lengthier the solution time gets. Therefore, the dimensions of the moving mesh region must be carefully selected to simultaneously ensure a good wake visualization and overall computational time while maintaining a reasonable computational time. Furthermore, practical considerations should be taken into account for the selection of the dimensions of the computational domain's outer region as well. The outer region is long enough in the streamwise direction to ensure smooth exit of the vortices through the outflow boundary. Figure 4 shows the developed computational domain and Table 4 provides insights into the selected dimensions. It should be mentioned that a turbulence length scale L_{t_scale} of 0.1 and a turbulence intensity I_t of 10% are used for the conducted simulations.
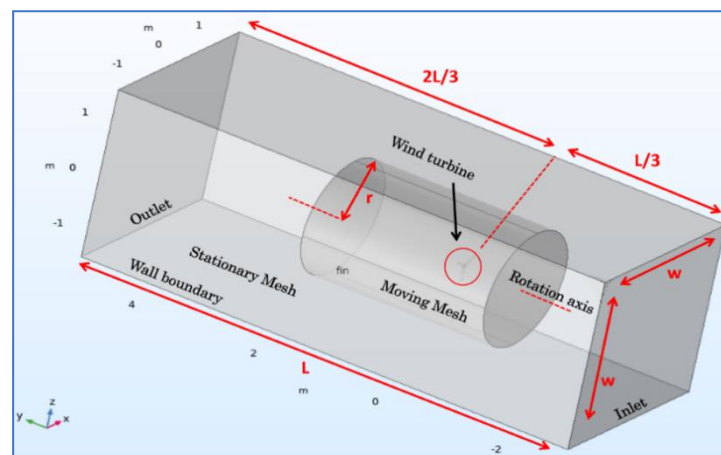

Figure 4. Simulation computational domain.

Table 4. Dimensional characteristics of the computational domain.

Parameter	Description
L	$\sim 40 \times Blade\ span$
W	$\sim 15 \times Blade\ span$
R	$\sim 5 \times Blade\ span$

Incorporating two noncongruent meshing types within the same fluid domain needs to be associated with the use of *identity pairs* in order to maintain the solution continuity, especially between elements within the adjacent *stationary* and *rotating mesh* domain surfaces. This safeguards that the solution is as smooth as possible over the intermediate mesh discontinuity. Table 5 encapsulates different boundary conditions and their corresponding equations at each boundary.

Table 5. Boundary conditions and their descriptions.

| Boundary/Governing Physics	Applied Condition	Representative Equation	Description
Wall boundary	Slip	$v = 0$ (zero normal velocity)	Used for the stationary outer walls of the computational domain. Specifies that the computational domain mimics the open-air conditions.
Rotating region	Sliding region	$u_{w2} = u_{w1}$	Used for the moving region near the rotating turbine geometry. The velocity of the wall u_{w2} is specified to match the rotational rate of the turbine u_{w1} by the designated rpm.
Fluid inlet	Velocity boundary condition	$u = U_\infty$	Used to specify a constant inlet/freestream velocity.
Fluid outlet	Pressure boundary condition	$p = p_{atm}$	Used to specify the pressure at the outlet.

3. Grid Dependence and Convergence Analysis

A grid sensitivity analysis is performed in order to make sure that the number of elements is sufficient to acurately depict the flow characteristics. A total of seven meshes are considered for this analysis, and the NACA0012 airfoil model is used. The turbine stresses in the three directions—x, y, and z—are computed and compared for all the considered mesh configurations. Table 6 shows more details about the conducted analysis, and more insights can be found in [53].

Table 6. Convergence analysis.

Mesh	Total Elements Number	X-Stress Percentage Change with Regards to Optimal Mesh (4)	Y-Stress Percentage Change with Regards to Optimal Mesh (4)	Z-Stress Percentage Change with Regards to Optimal Mesh (4)
1	584,399	31.19%	40.30%	31.21%
2	981,630	17.53%	20.25%	17.56%
3	1,174,105	13.78%	14.83%	13.78%
4 (optimal)	1,571,296	-	-	-
5	1,759,516	0.39%	0.50%	0.42%
6	1,962,624	0.55%	0.84%	0.08%
7	2,120,669	0.81%	0.91%	0.76%

Additionally, Figure 5 shows the meshed computational domain for both meshes 1 and 4, of which the overall number of elements is approximately 5.84×10^5 and 1.57×10^6, respectively. The legend represents the element quality, where a mesh element is colored green if its corresponding quality is good. On the other hand, yellow and orange elements have compromised-to-poor quality. The quality of mesh elements in COMSOL is measured through the skewness level. In other words, the more skewed an element becomes, the less its quality. Inverted elements are elements with very low quality. A high element aspect ratio is also considered detrimental to the mesh quality; therefore, a maximum threshold of three is set. These should be avoided since they cause high condition numbers for the Jacobians, which, in turn, leads to convergence complications. A 'perfect' element has a quality of one. It should also be mentioned that an automatic wall treatment that

is associated with the low Re k-ε turbulence model was used. This CFD feature ensures an automatic selection of a robust wall function or a low Reynolds number formulation, which resolves the velocity profile all the way to the wall. Additionally, it is clear that mesh density is remarkably different between the stationary domain and the rotating domain near the turbine; for that, the creation of the mesh was first calibrated for fluid dynamics with a finer, predefined mesh type. Then the element size parameters comprising the maximum element size, the minimum element size, and the maximum element growth rate are adjusted in the rotating domain, which is ~6–8 times denser than the stationary domain.

(**a**)   (**b**)
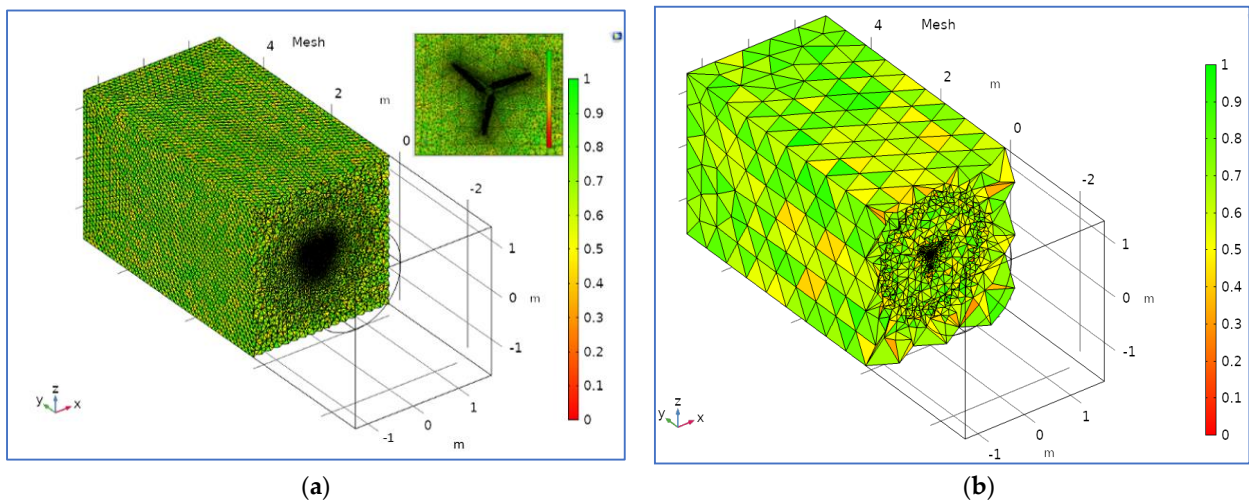
Figure 5. Meshed computational domain for (**a**) mesh 4 and (**b**) mesh 1.

4. Results and Discussion

4.1. Blade Shape Effect on SSWT Performance

4.1.1. SSWT Performance Assessment with Varying Blade Shapes

In order to get the maximum energy out of wind power, a good performance of the aerodynamic components of the wind turbine plays a critical role. Designing an optimal blade able to generate the optimal lift and, consequently, a high torque output goes in line with its size and the corresponding characteristics and factors of the functioning conditions it is subject to; namely, the density and speed of the operational wind, the overall surface area, the flow profile, and turbulence characteristics, among others. In this section, the torque and power of the aforementioned tapered and rectangular blade configuration are assessed by jointly exploring the performance of four airfoil profiles—NACA4412, NACA4415, NACA0012, and NACA0015—for each individual blade shape. The flow around the turbine is investigated and the generated torque is calculated using the following expression:

$$\vec{T} = \vec{r} \times \vec{F} \tag{5}$$

where $\vec{T}$ represents the turbine's generated torque, $\vec{r}$ is the distance between the tip of the turbine's blade and the rotational center, and $\vec{F}$ denotes the force of the fluid flow responsible for the rotation of the structure. The latter is obtained from the integration of the stress tensor over the turbine's surface area. Thereafter, the corresponding power is computed as:

$$P = T\omega_r \tag{6}$$

where T corresponds to the magnitude of the generated torque and ω_r represents the angular rotational speed.

The rotation of the overall geometry of various rotor-based systems—namely, helicopter rotors, propellers, and wind turbines—produces the wake phenomenon through

the shedding of vortices onto the downstream. The wake is characterized by a region in which the wind speed is reduced and the turbulence intensity is increased. The physics of wake formation can be understood by considering the various physical mechanisms that contribute to the phenomenon. First, the shedding of vortices: the rotation of the turbine blades disturbs the airflow and results in the vortices being shed downstream of the turbine. The pressure differential between the blade's upper and bottom surfaces, producing areas of high and low pressure, is what causes these vortices to develop. The second characteristics of this phenomenon is turbulence. In fact, turbulence intensity in the wake zone is greater than that in the freestream because of the dynamic interactions between fluids with high and low momentum. Third, pressure differences around the turbine blades can also engender flow separation, where the flow separates from the surface of the blade and creates a region of low pressure behind the blade. Dominant vortices of the wake specific to horizontal axis wind turbines take the form of counter rotating helical vortex pairs, constituting the vortex shed of each turbine blade's root and tip [58]. The aforementioned vortices have a supreme role in the further development of the wake in the downstream direction of the rotating structure. In fact, as this helical structure moves further from the rotating turbine, the magnitudes of the shed vortices are attenuated where the flow is solved in larger mesh elements, resulting in a decrease of flow magnitude as it leaves the computational domain. Figure 6 depicts the formation process of the helical vortex structure in the downstream of the rotating turbine for the case of rectangular blades with NACA4412. A similar overall helical structure is observed for the various studied shapes.

Considering the previously mentioned airfoil profiles, the torque and aerodynamic power of each profile are calculated while considering both the rectangular and the tapered configurations with similar twist distribution. It should be mentioned that while the twist distribution is assumed to be the same for all the cases studied, the authors acknowledge, however, that it might not be optimal for all the considered blade shapes and airfoil profiles. Nevertheless, this was considered for comparison purposes. Figure 7 showcases the steady-state torque values for the eight cases investigated and Table 7 shows the generated torque, power, and power density for each of the considered aerodynamic configurations. The results show that both airfoil and blade shape have a major influence on the performance of SSWTs, with the shape of the blade being more important. Visibly, it is shown that for the four cases of the airfoil profiles considered, the rectangular blade shape outperforms the tapered blade configuration. Additionally, for the considered operating conditions, the output power values show that the most effective configuration is when the rectangular blade shape is associated with the NACA4412 airfoil profile, yielding a power output of 2.452 W. Conversely, the worst configuration from the energy output perspective is when the tapered blades and a NACA4415 are combined. Furthermore, a decrease of approximately 17.96% of the generated power is noted for the case of the optimal airfoil (NACA4412,) when the blade shape is changed from a rectangular to a tapered profile. On the other hand, the percentage difference between the most-performing and the least-performing airfoil cases is 7.60% and 6.32% for the tapered and rectangular blade shapes, respectively. It is important to mention that while the NACA4412 yields the highest power compared to the other airfoil profiles considered for both the tapered and rectangular blade configurations, the least power generated for the tapered blade shape configuration corresponds to the NACA4415 airfoil, while lower power is obtained when the NACA0015 profile is used for the rectangular blade shape. This highlights the high coupling and interdependence of the geometric characteristics of the turbine blades and their effect on overall SSWT performance. Therefore, although some studies used two-dimensional techniques to predict the performance of SSWT blades, the overall blade shape effect on the yield is not captured in such efforts. This stresses the importance of three-dimensional analyses, where the entire bladed geometry is considered, rather than the two-dimensional assessments, where the blade is assumed to have an infinite aspect ratio and, consequently, 3D flow effects and blade shape influence are not captured.
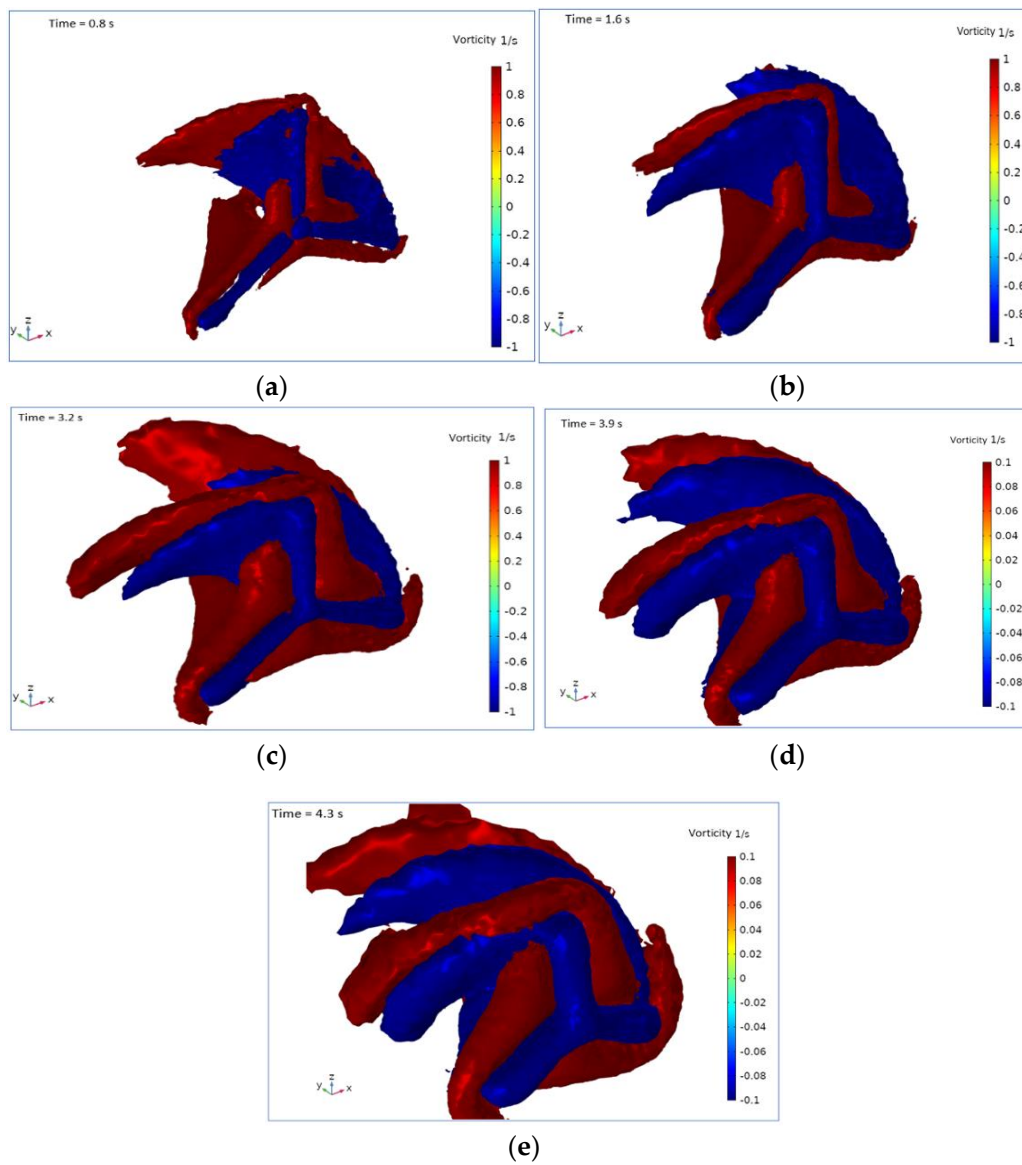
Figure 6. Time frames depicting the formation of the near-wake helical vortex pair structure in the downstream of the rotating turbine at (**a**) t = 0.8 s; (**b**) t = 1.6 s; (**c**) t = 3.2 s; (**d**) t = 3.9 s; (**e**) t = 4.3 s.
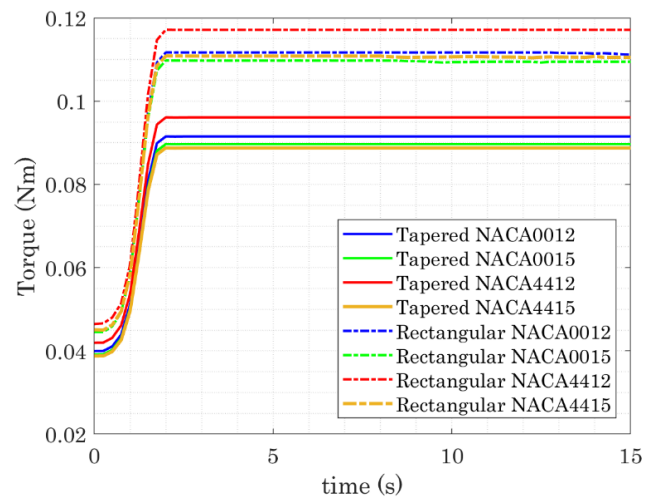
Figure 7. Steady-state torque.

Table 7. Power generation for the studied blade shapes and corresponding airfoil profiles.

| Blade Shape	Airfoil Profile	Torque (Nm)	Power (W)	Power Density (W/m^2)
Tapered	NACA0012	0.0915	1.919	9.77
	NACA0015	0.0897	1.878	9.56
	NACA4412	0.0961	2.012	10.25
	NACA4415	0.0888	1.859	9.46
Rectangular	NACA0012	0.1117	2.339	11.91
	NACA0015	0.1097	2.297	11.70
	NACA4412	0.1171	2.452	12.49
	NACA4415	0.1108	2.320	11.82

In order to have more insights into the effect of blade shape on flow behavior, x-z cut plots of the flow velocity around the turbine are generated and illustrated in Figure 8. A uniform legend is used, with a display of the maximum and minimum velocity values, depicted by the up- and down-facing arrows; details about the turbines' geometric characteristics are stated in Figure 1 and Table 1. The flow tendencies and velocity magnitude distributions around the geomery suggest that higher flow velocity magnitudes lie near the rotating tip, while lower velocity magnitudes are close to the hub. Furthermore, the results show that, when a freestream velocity of $U_\infty = 4$ m/s is used, the flow relative velocity values are constanty higher than the freestream flow velocity value. This is because the obtained relative velocity profile $\vec{U}_{rel}$ is a result of the freestream velocity in addition to the acceleration of the flow due to the rotating motion. Mathematically, it is given as:

$$\vec{U}_{rel} = \vec{U}_\infty + r_t\vec{\omega} \tag{7}$$

It can also be seen that the flow's maximum values attained around the turbine are constantly higher for the rectangular shape when compared to the tapered blade shape, regardless of the airfoil profile case. Furthermore, it can be seen that the NACA4412 airfoil profile yields the higher relative flow velocity of $U_{rel} = 7.84$ m/s when the rectangular blade shape is considered and $U_{rel} = 7.11$ m/s when the tapered blade shape is used. Since the kinetic energy of the turbine depends on the velocity of the flow, higher flow velocities should automatically translate to a higher power potential of the rectangular blades over the tapered one for the selected twist and operating conditions.

The vorticity behavior investigations should go hand in hand with the velocity field examinations since they provide more detailed insights into the transient behavior of the flow when interacting with the moving geometry. Therefore, an x-z plot view of the vorticity is provided in Figure 9a,b of both the rectangular and tapered blade geometries when the NACA4412 airfoil is considered. Additionally, in order to explore the turbulent wake flowing downstream of the wind turbine and the evolution of the helical tip vortices induced by the rotating turbine blades, a z-y plot view of both airfoil profiles and blade geometries is also incorporated in Figure 9c,d. It can be seen that the vorticity magnitudes that result when the rectangular configuration is used are greater than those obtained when the tapered blade shape is considered. Moreover, a more pronounced separation at the tip is noticed for the case of the rectangular blades compared to its tapered counterpart. The z-y plots show that the blade shape has a great influence on the far-wake vorticity behavior as well, where a clear downstream wake structure is noticed for the tapered blade case, while more attached vortices are formed when the rectangular blade geometry is considered, resulting in a continuous wake shedding. This can be explained by the fact that the magnitude of the vorticity is strongly analogous to the intensity of the vortices formed due to flow separation. When the flow separates, vorticity is generated around the region of separation, and the magnitude of the vorticity is proportional to the strength of

the vortex. In general, the larger the magnitude of the vorticity, the stronger the vortex and the more significant the effect on flow downstream. Consequently, flow separation can lead to the formation of vortices with high vorticity magnitudes.
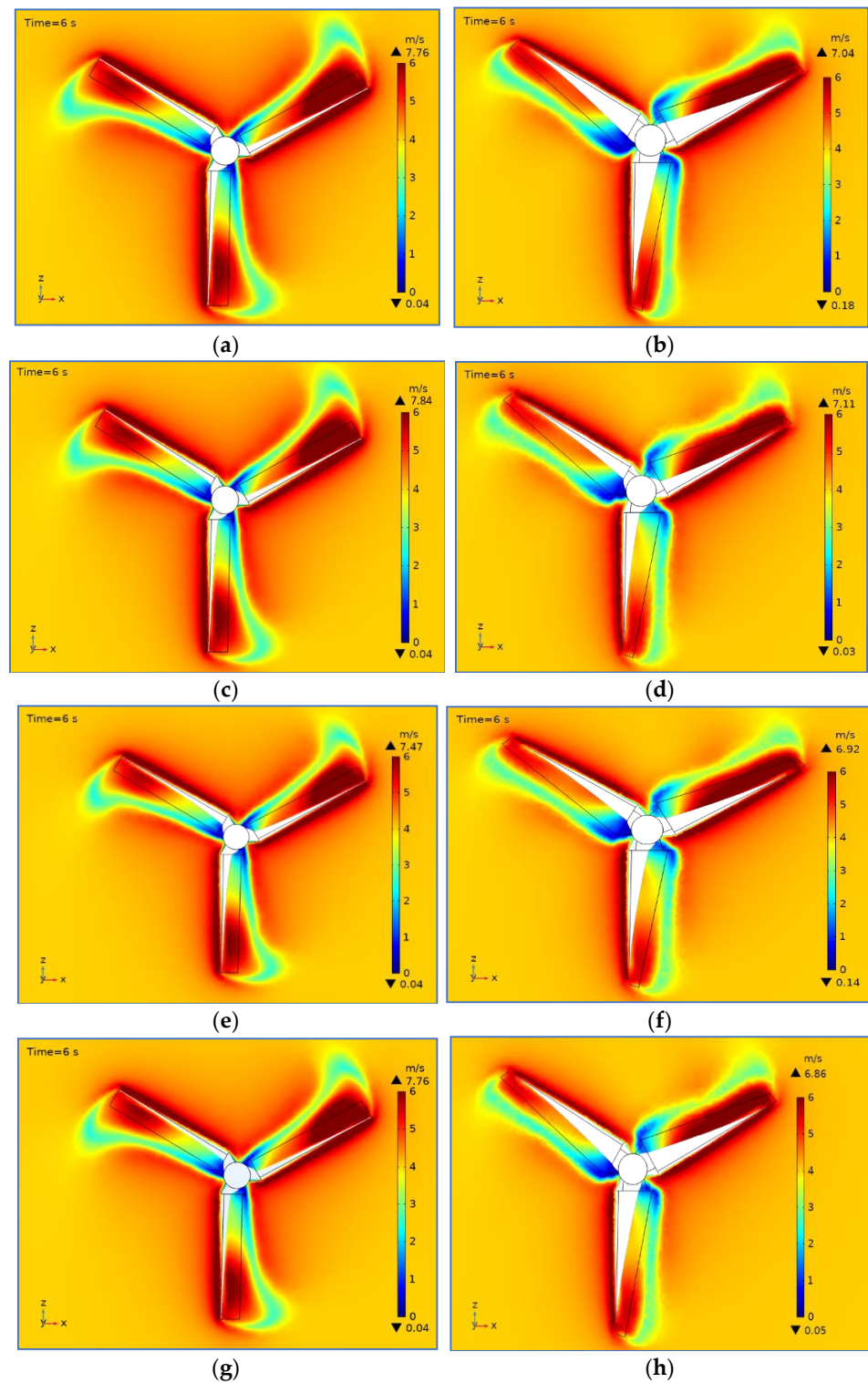
Figure 8. x-z projection of the velocity profile for the rectangular (**a**,**c**,**e**,**g**) and tapered (**b**,**d**,**f**,**h**) configurations with the airfoil profile: (**a**,**b**) NACA0012; (**c**,**d**) NACA4412; (**e**,**f**) NACA0015; and (**g**,**h**) NACA4415.
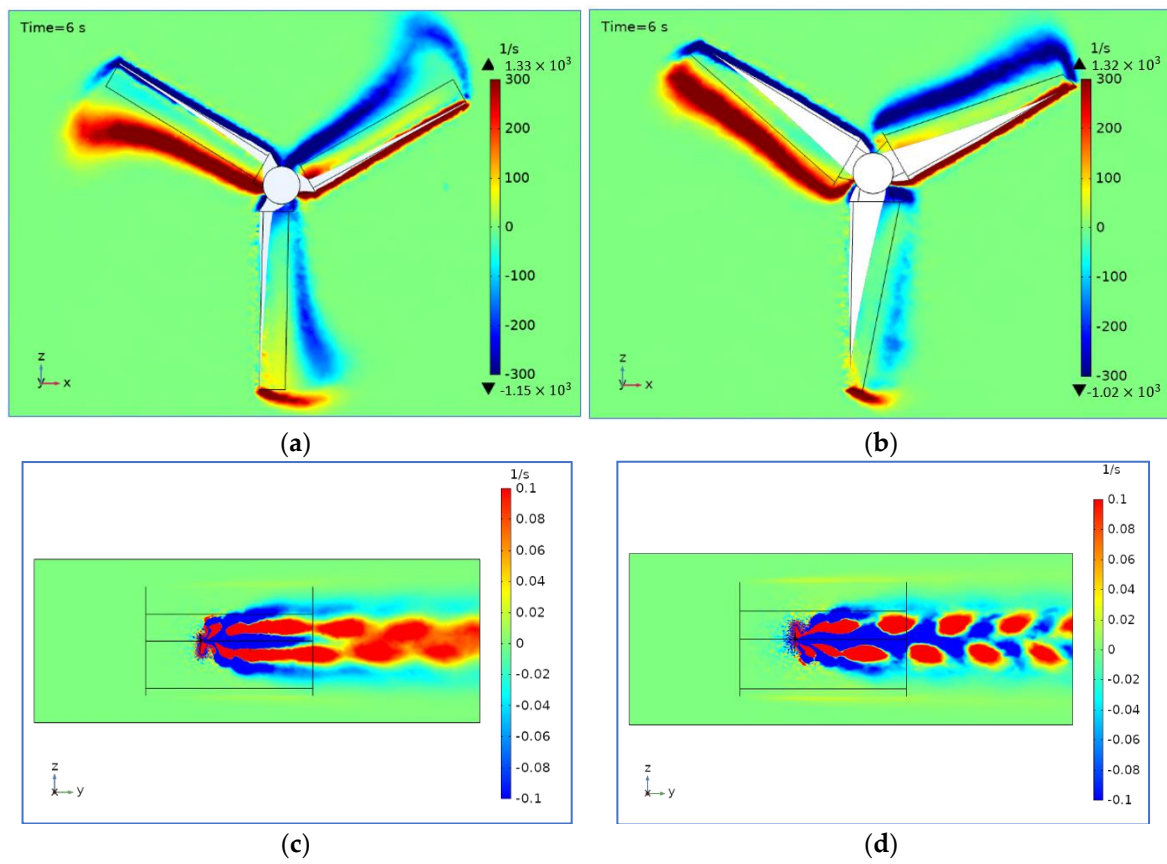
Figure 9. x-z view of the vorticity profile for the (**a**) rectangular and (**b**) tapered configurations (NACA4412 airfoil), and z-y view of the vorticity profile for the (**c**) rectangular and (**d**) tapered configurations.

To understand the flow behavior across a single blade of the rotating turbine, three different cut plots are generated at three locations: near the hub, at the mid-span, and near the blade tip, and the flow results are presented in Figure 10. First, it can be seen that for the case of a rotating geometry, where the flow is characterized by more significant rotation-induced turbulence and the flow direction witnessed by the blade is constantly changing because of the interactions between the flow and the moving structure, the stream profile therefore does not always look as predictable as that of the 2D airfoil analyses. Additionally, looking at the vorticity magnitudes, it can be noted that the rectangular blade configuration continuously yields higher magnitudes, which might explain the continuous vortex shedding displayed in Figure 9, where the vortices with higher magnitudes contributed to making the shedding look more continuous. Furthermore, an early separation is seen near the hub for both configurations since the preset angle at that specific location is not necessarily aerodynamically optimal. In fact, the main design consideration of the blade part adjoining the hub is generally maintaining structural integrity and preventing blade failure rather than aerodynamic efficiency. Additionally, twist angle near the hub of the blade is often designed to be high to ensure that the blade operates at a more optimal angle of attack, given the slower velocity of the wind near the hub. However, this high twist angle can lead to the formation of a region of high pressure near the hub, which can cause premature flow separation and stall of the blade.

However, as one moves away from the hub in the direction of the tip, more aerodynamic efficient design considerations take place and, as a consequence, the flow profile looks more conventional, with the separation occurring at the trailing edge.
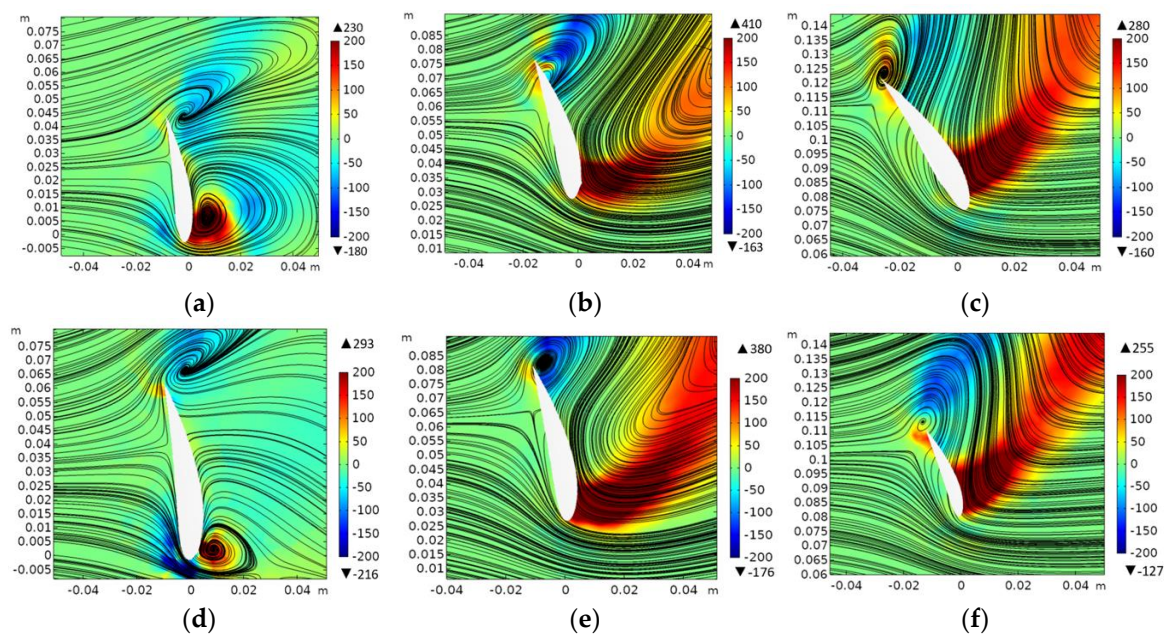
Figure 10. Blade cuts showing the vorticity contours and velocity streamlines of the flow across the blade (**a**,**d**) near the hub, (**b**,**e**) mid-span, and (**c**,**f**) near the tip for rectangular (**a**–**c**) and tapered (**d**–**f**) configurations.

4.1.2. Effect of Blade Shape on Aerodynamic Loads

Turbine blade deterioration can take place in operating conditions characterized by steady types of flow as well as when undergoing unsteady turbulent flow types. Consequently, a major challenge that is faced by wind turbine designers is to ensure that the turbine has a good durability, making it capable of enduring harsh operating environments without compromising very much on its aerodynamic efficiency. Research efforts have shown that turbine blades are the components that are more prone to time-induced harm and structural wearing out among all other constituent parts of a wind turbine [59]. Generally, small-scale turbine blades are manufactured using composite materials or are 3D printed. Advancements in manufacturing made it possible to use more over-the-counter components that are, simultaneously, cheap and widely accessible. Despite the remarkable efficiency and production power this has yielded, additively manufactured blades, however, are more inclined to hygrothermal impacts, resulting in quick weakening and aging, especially with fluctuating temperature and humidity conditions [60]. Hence, the compromised blades' overall strength makes them more susceptible to damage, especially when undergoing loading stresses and coupled loading flow conditions. With this in mind, it is therefore very important to investigate closely the stresses that rotating turbines undergo in order to attain a long life cycle for an SSWT.

The x, y, and z local distributed stresses that a single SSWT blade is subject to are, therefore, computed and depicted in Figure 11. Their values are obtained by performing a surface integration of the flow force loadings around the overall surface of a single blade. They are a direct result of the aerodynamic loads that the turbine blade is subject to. Consequently, blades with extremely high resulting stress values are more likely to be susceptible to structural wearing out and deterioration. It should be mentioned that since the computational domain is symmetrical with respect to the y-axis, which is the rotational axis, the obtained root mean square (rms) values of the x and z stress values are very similar. The results show that tapered blades faced less stress load magnitudes than their rectangular counterparts. In fact, decreases of approximately 42.21% in the case of NACA4412, 42.49% for NACA4415, 40.64% when NACA0015 is considered, and 42.49% in the case of NACA0012 for both x and z stresses take place when the blade shape is changed from rectangular to tapered with identical overall surface area. Similarly in the y

direction, rectangular blade shapes continue to yield higher stress magnitudes for all the airfoil profiles.
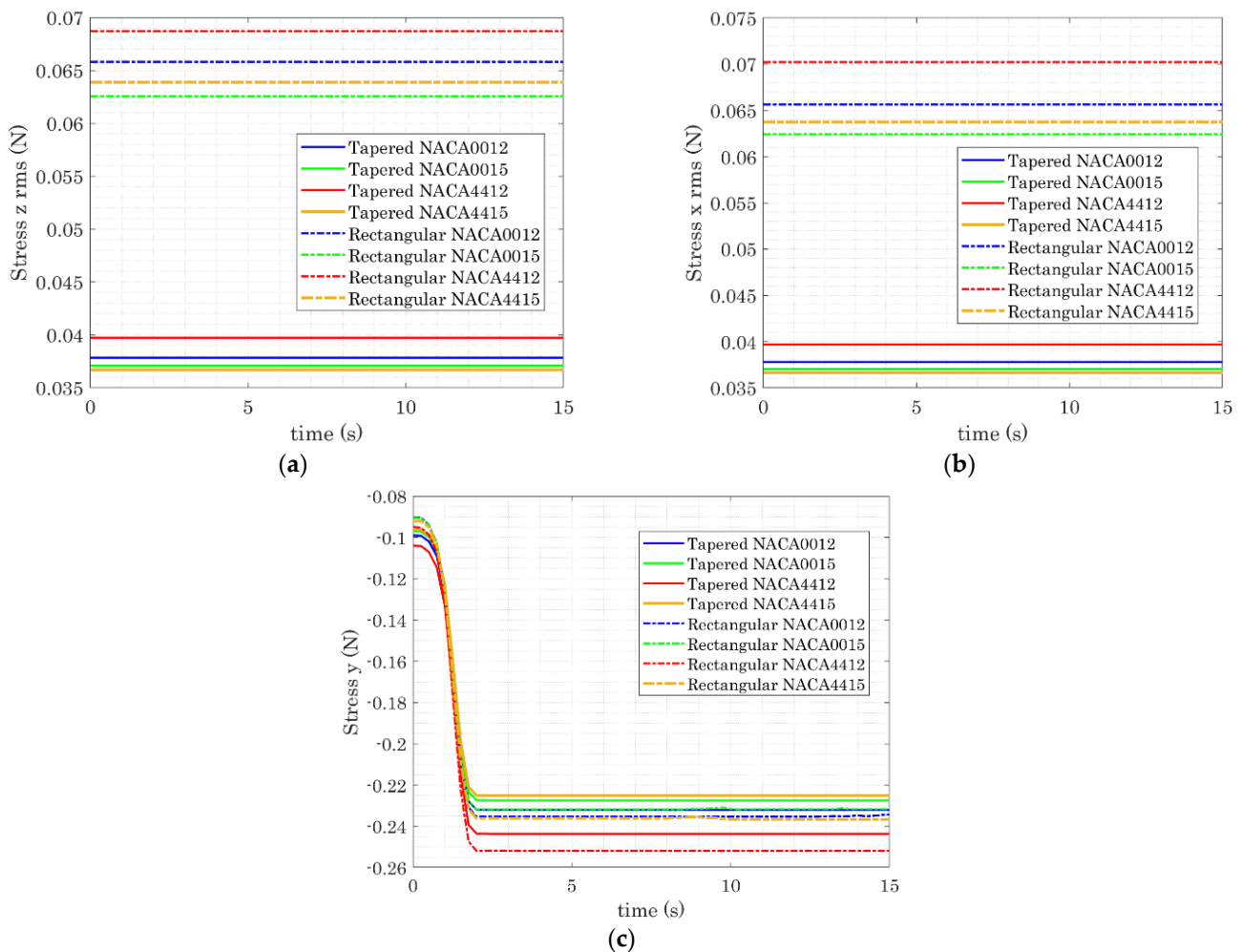
Figure 11. (**a**) x-stress rms, (**b**) z-stress rms, and (**c**) y-stress undergone by a single SSWT blade.

In order to understand the reason behind the tapered blades resulting in overall less stress magnitudes compared to the rectangular blade shapes, the pressure distribution is also investigated using identical flow conditions, which are shown in Figure 12 for both the rectangular and tapered shape consigurations when the NACA4412 airfoil profile is considered. In view of the fact that pressure is a function depending on flow velocity, the blade portions lying near the hub have low pressure magnitudes. Conversly, moving further away from the hub, the values of the pressure increase, attaining the highest value at the turbine blade tip. The negative and positive pressure distributions generated on the suction and pressure sides of the blades, respectively, are tabulated. One can see that, near the blade tip, the air is characterized by a faster motion, resulting in higher pressure magnitudes for both tapered and rectangular configurations. However, the large stress values specific to the rectangular configuration case can be explained by the fact that maintaining the same chord along the blade span results in a larger surface area exposed to higher pressure magnitudes at the tip. On the other hand, for the tapered blade case, the chord length is decreased, resulting in a smaller surface area at the tip region compared to the hub. Consequently, the area exposed to high pressure magnitudes on the tip side is decreased in the case of the tapered blade, which automatically results in less stress magnitudes overall. Additionally, it can be seen that in the case of the tapered blade configuration, the higest positive pressure magnitude lies at the tip region, while the

highest suction pressure magnitude is recorded near the hub. However, for the rectangular blade shape, an additional high magnitude region also lies mid-blade for the suction side, as can be seen in Figure 12a.
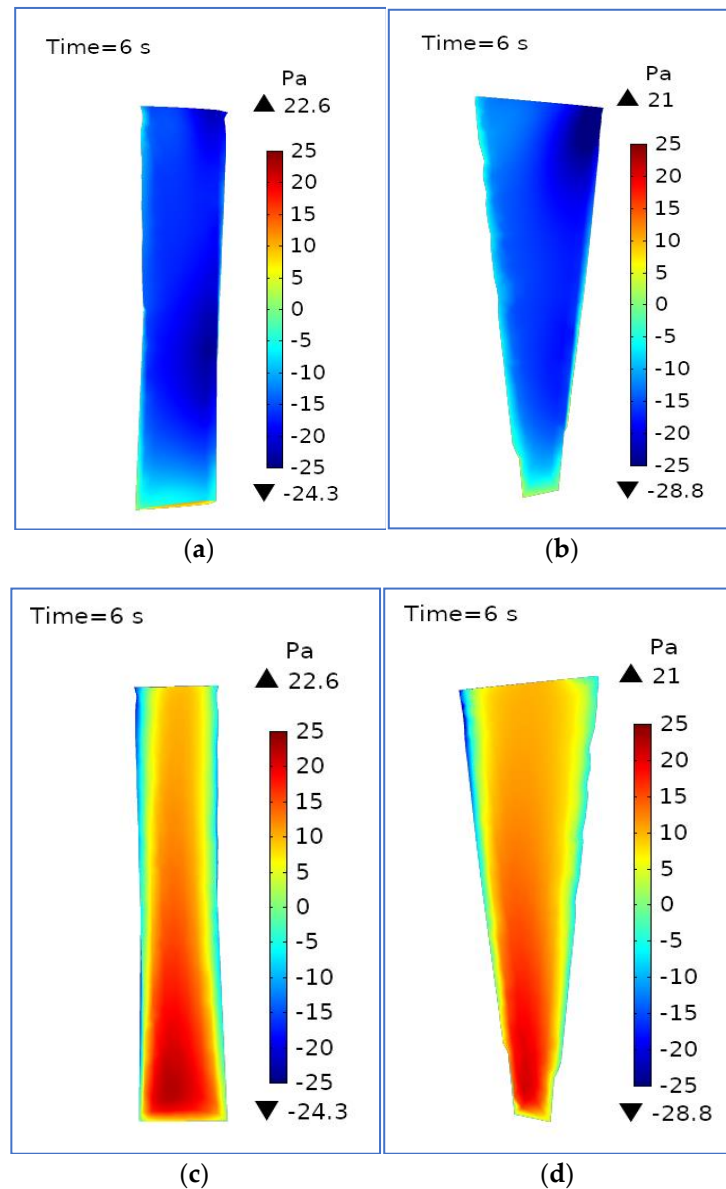

Figure 12. Negative suction pressure and positive pressure distributions for (**a**,**c**) rectangular blades and (**b**,**d**) tapered blade configurations.

4.2. Twist Distribution Effect on SSWT Performance

In this section, the influence of twist angle distribution on the overall efficiency of the SSWT is explored. The different linear and nonlinear twist distributions that are depicted in Figure 3 are considered. The details of each twist distribution are provided in Section 2.1 and a summary of the differences between each configuration is provided in Table 2. The performance of the SSWT with rectangular shaped-blades associated with the NACA4412 airfoil is examined while considering the same aforementioned flow conditions and solver configurations. Figure 13 shows the velocity of the flow around the rotating turbine when different twist configurations are considered. The results show that higher flow velocities are obtained in the case of Fit A twist distribution, while the lowest flow velocities correspond to Fit E distribution. Additionally, one can notice that higher relative flow velocity values generally correspond to the nonlinear twist distribution configurations.

However, it is important to mention that the second highest flow velocity magnitude is obtained when linear twist configuration Fit F is considered.
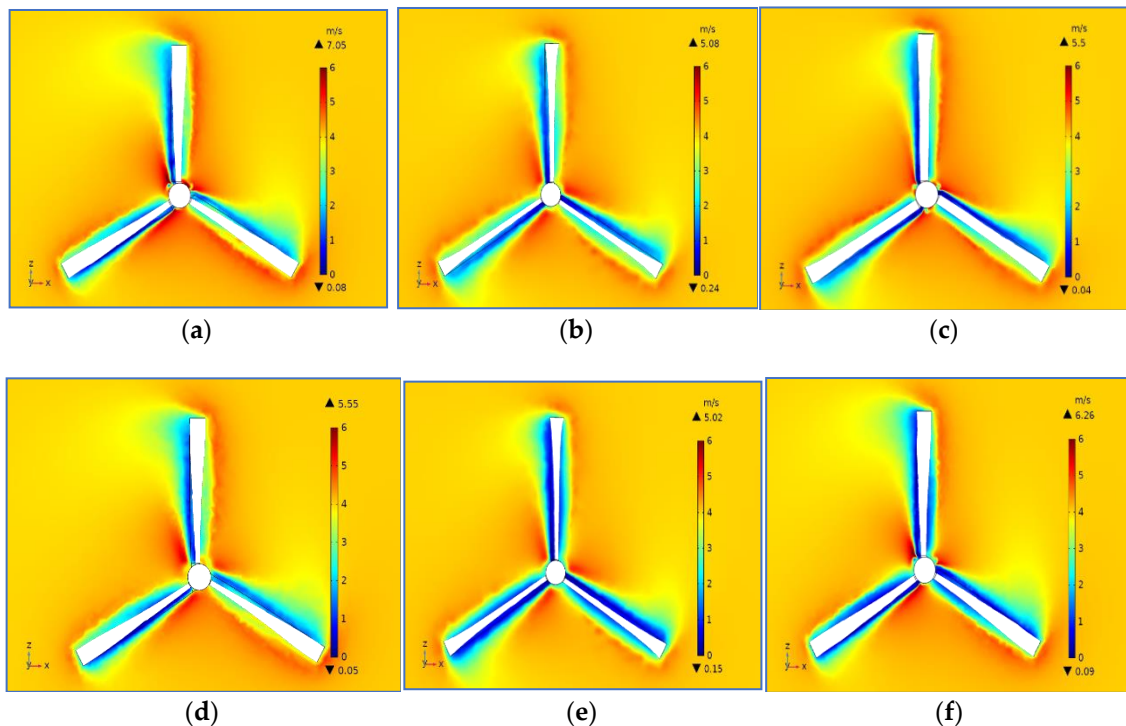

Figure 13. Velocity profiles of the flow surrounding the rotating turbine for (**a**) Fit A, (**b**) Fit B, (**c**) Fit C, (**d**) Fit D, (**e**) Fit E, and (**f**) Fit F.

The blade span cut plots are also generated considering the three twist distributions of Fit A, Fit B, and Fit C in Figure 14. It can be seen that, generally, the vortices in mid-span and near the tip are higher than those yielded at the hub. Furthermore, it can be seen that Fit A yields higher vorticity magnitudes, followed by Fit C with the second-highest magnitudes across the blades, while Fit B results in lower magnitudes throughout the blade span overall. Additionally, an early separation takes place at the near-hub portion of the blade. However, the flow reattaches approaching the tip.

In order to have a good assessment of the yielded performance obtained when considering each twist distribution, the steady-state torque is computed and is shown in Figure 15. Further, the corresponding power and power density are computed for each configuration and are provided in Table 8. The results show that the highest power of 2.496 W corresponds to twist distribution Fit A. Linear Fit F has the second-highest power of 2.449 W, while the lowest power generation is obtained with linear Fit F. Furthermore, while a smaller slope is more favorable in the case of the linear distributions among the cases considered, the nonlinear twist angle distribution characterized by a medium steepness yields the highest power production. The overall assessment of the obtained power values suggests that nonlinear twist distributions are favorable in terms of power production. However, linear twist distributions can be as competitive only if a good steepness slope value is considered. Nevertheless, linear distribution with a very high slope can result in the stall phenomenon, where the lift decreases from its optimal angle of attack range and, consequently, the overall performance potential of the turbine is compromised. In fact, the latter reasoning can be said for all twist distributions, where, even though in a reseach effort [34] it was shown that to make starting easier, there should be an increase in the chord/twist values at the root part of the blades, a very large twist at the root, however, is not practical both aerodynamically, since it may result in the stall phenomenon prematurely,

and also in terms of manufacturing, since the fabrication of a blade with high twist values at the root is not possible [61].
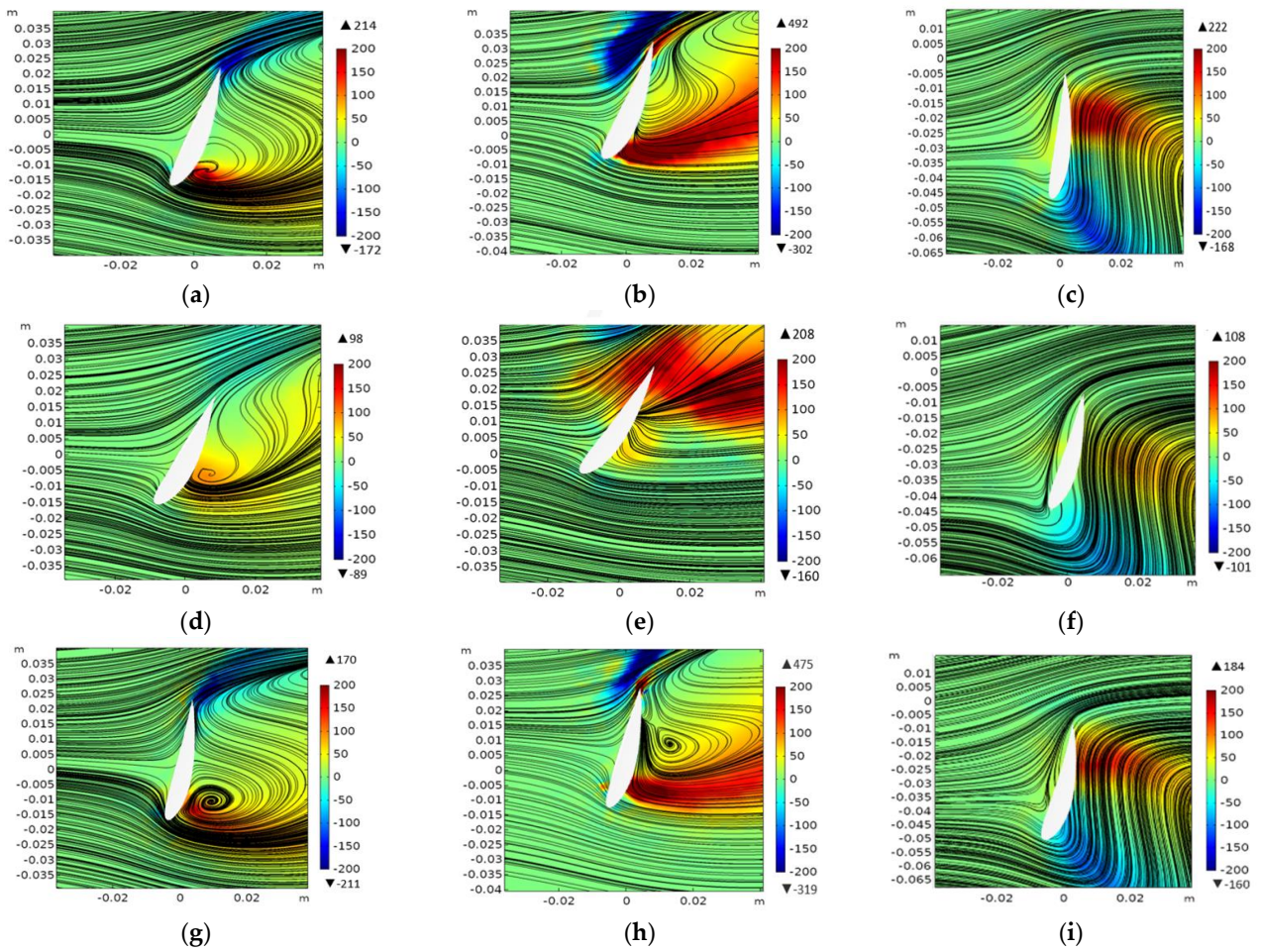
Figure 14. Blade cuts showing the flow across the blade for (**a**,**d**,**g**) the cross-section near the hub, (**b**,**e**,**h**) the mid-span cross-section, and (**c**,**f**,**i**) the cross-section near the tip for Fit A (**a**–**c**), Fit B (**d**–**f**), and Fit C (**g**–**i**) configurations.
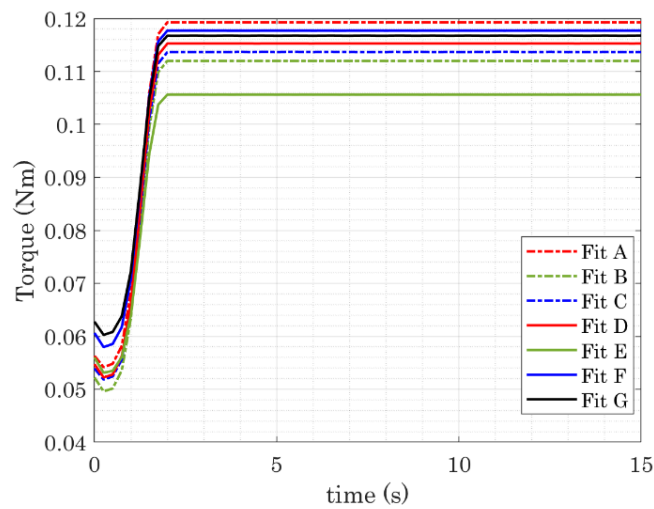

Figure 15. The steady-state torque obtained for different twist distributions.

Table 8. Power generation for the studied twist distributions.

Distribution Profile	Torque (Nm)	Power (W)	Power Density (W/m²)
Fit A	0.1192	2.496	12.71
Fit B	0.1119	2.343	11.93
Fit C	0.1136	2.379	12.12
Fit D	0.1153	2.414	12.29
Fit E	0.1056	2.211	11.26
Fit F	0.1177	2.449	12.47
Fit G	0.1167	2.444	12.45

The negative suction pressure and positive pressure distributions that the turbine is subject to are also assessed for various twist distributions. Figure 16 shows the results for Fit D, Fit E, and Fit F in order to assess how pressure distribution tendencies are affected by linear slope magnitude. It can be seen that highest pressure values obtained correspond to the twist distribution with the highest linear slope. In contrast, lower pressure magnitude values are obtained when the less steep slope is used for the twist angle distribution.
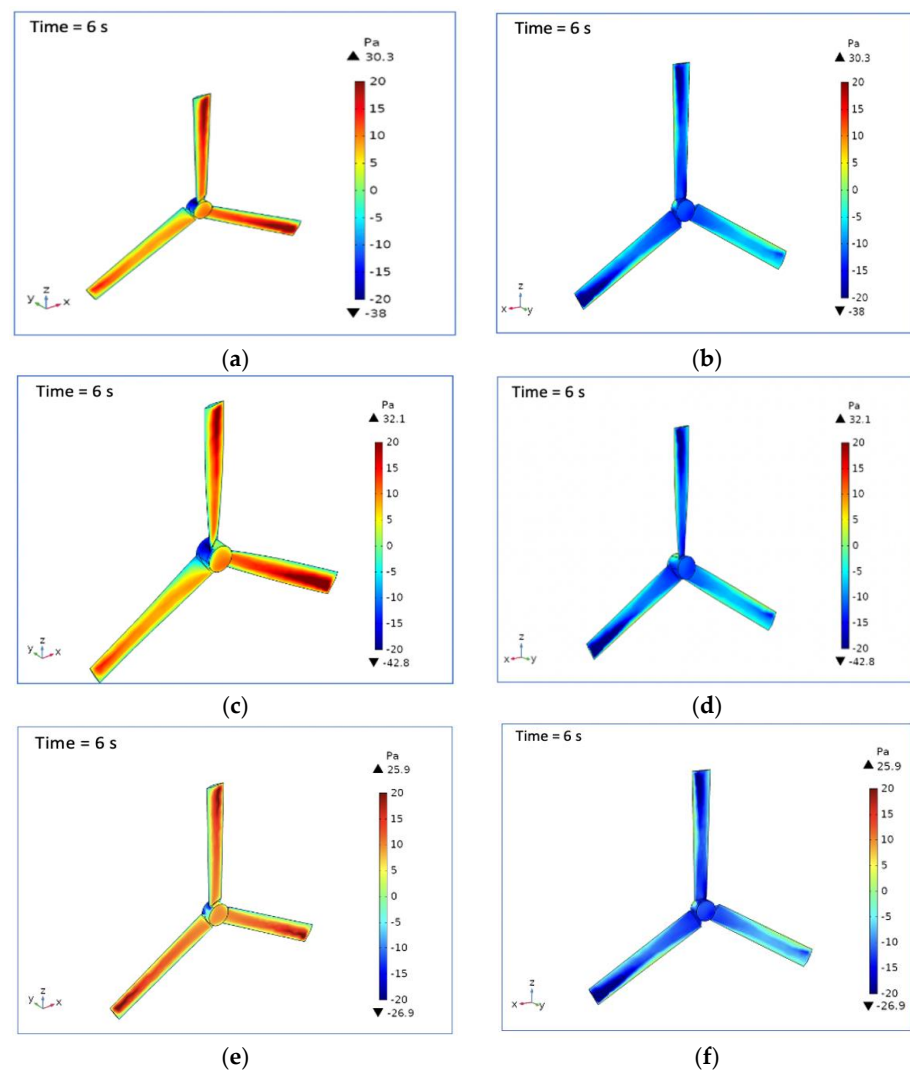
Figure 16. Negative suction pressure and positive pressure distributions for (**a**,**b**) Fit D, (**c**,**d**) Fit E, and (**e**,**f**) Fit F.

In line with the pressure distribution predispositions, the stresses that the turbine is subject to are calculated and presented in Figure 17. From the obtained values, it is clear that steeper twist distribution results in higher stress values if both the studied linear and nonlinear configurations are considered. However, the linear twists constantly yield higher stress magnitudes for the x, y, and z directions compared to their nonlinear counterparts. Additionally, it can be deduced that a good twist distribution can simultaneously ensure high steady-state torque generation while guaranteeing reasonable induced stress, and is, therefore, a good selection aerodynamically and structurally. For instance, Fit A yielded the highest torque and resulted in the second-lowest amount of stresses that the blade undergoes.
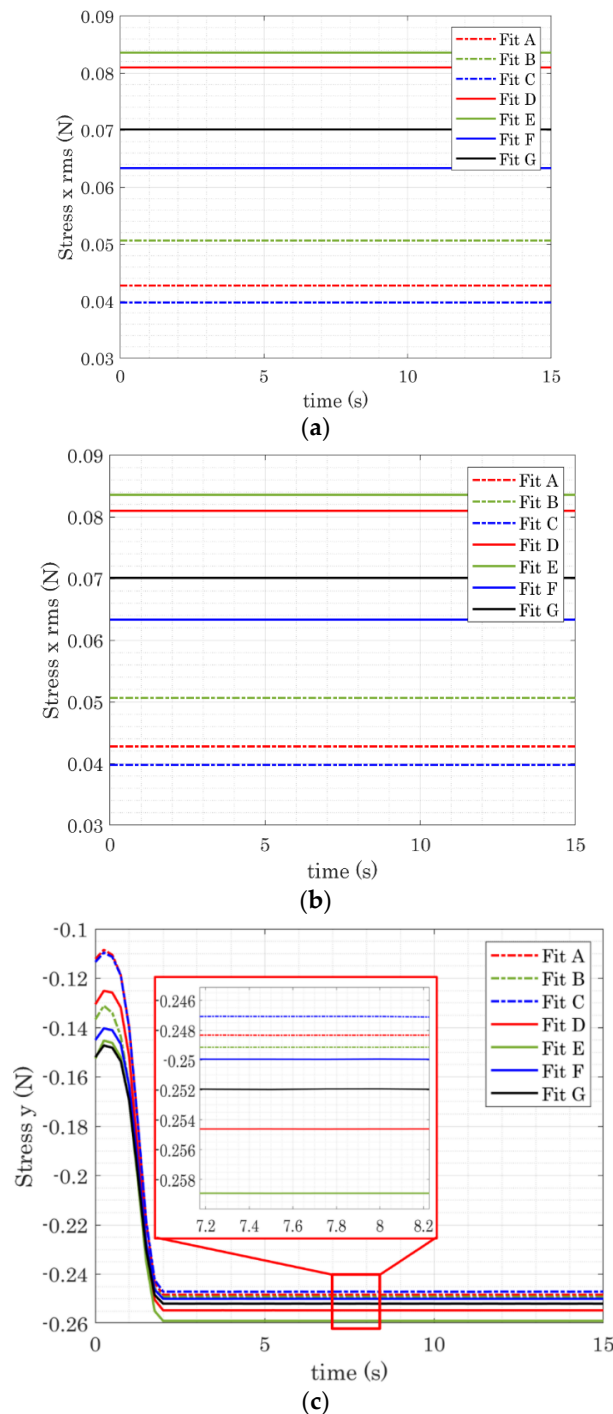

Figure 17. (**a**) x-stress rms, (**b**) z-stress rms, and (**c**) y-stress resulting from a single SSWT blade.

5. Conclusions

In this work, the effects of different design and geometric characteristics of SSWTs on their aerodynamic performance is assessed using high-fidelity CFD analyses, where the full Navier–Stokes equations were solved and a mesh convergence analysis was conducted. Rectangular and tapered blade shapes as well as different linear and nonlinear twist angle distributions characterized by different steepness and slope traits were explored. For the studied operating and geometric conditions considered, NACA4412 yielded the highest power in comparison to the other airfoil profiles for both the tapered and rectangular blade configurations. The least power generated by the tapered blade shape configuration corresponds to the NACA4415 airfoil, while a lower power was obtained when the NACA0015 profile was used for the rectangular blade shape. For the considered flow characteristics, the power values showed that the most effective configuration is the rectangular blade shape with the NACA4412 airfoil profile, generating a power output of 2.452 W. In addition, it was revealed that while the rectangular blade shape is favorable in terms power production for the studied conditions, it nevertheless resulted in higher blade stresses. Therefore, a compromise between structural and aerodynamic blade characteristics is necessary to attain an aerodynamically effective and structurally robust SSWT design.

The twist distribution assessments suggested that the nonlinear twist distribution is advantageous in terms of power production when considering the studied cases. However, linear twist distributions can be a good option as well provided that a good distribution slope value is considered. Considering the cases in hand, steeper twist distributions resulted in higher stress values for both linear and nonlinear configurations. However, linear twists constantly yielded higher stress magnitudes for the x, y, and z directions compared to nonlinear configurations. Therefore, a favorable twist distribution can concurrently ensure high steady-state torque generation while guaranteeing reasonable load-induced stresses, and is therefore a good selection aerodynamically and structurally, as is the nonlinear twist for Fit A.

Author Contributions: Conceptualization, S.B.A. and A.A.; methodology, W.Y. and S.B.A.; software, W.Y.; validation, W.Y.; formal analysis, W.Y., S.B.A. and A.A.; investigation, W.Y., S.B.A. and A.A.; resources, A.A.; writing—original draft preparation, W.Y.; writing—review and editing, S.B.A. and A.A.; visualization, W.Y., S.B.A. and A.A.; supervision, S.B.A. and A.A.; project administration, A.A.; funding acquisition, S.B.A. and A.A. All authors have read and agreed to the published version of the manuscript.

Data Availability Statement: Data will be made available on reasonable request.

Conflicts of Interest: The authors declare that they have no conflict of interest.

References

1. Lim, C.W. Design and manufacture of small-scale wind turbine simulator to emulate torque response of MW wind turbine. *Int. J. Precis. Eng. Manuf. Green Technol.* **2017**, *4*, 409–418. [CrossRef]
2. Rehman, S.; Alam, M.M.; Alhems, L.M.; Rafique, M.M. Horizontal axis wind turbine blade design methodologies for efficiency enhancement—A review. *Energies* **2018**, *11*, 506. [CrossRef]
3. Hansen, M.O. *Aerodynamics of Wind Turbines*; Routledge: London, UK, 2015.
4. Amet, E.; Maître, T.; Pellone, C.; Achard, J.L. 2D numerical simulations of blade-vortex interaction in a darrieus turbine. *J. Fluids Eng.* **2009**, *131*, 111103. [CrossRef]
5. Saryazdi, S.M.E.; Boroushaki, M. 2D numerical simulation and sensitive analysis of h-darrieus wind turbine. *Int. J. Renew. Energy Dev. (IJRED)* **2018**, *7*, 23–34. [CrossRef]
6. Hoogedoorn, E.; Jacobs, G.B.; Beyene, A. Aero-elastic behavior of a flexible blade for wind turbine application: A 2D computational study. *Energy* **2010**, *35*, 778–785. [CrossRef]
7. Pardo, D.R.; Branner, K. Finite element analysis of the cross-section of wind turbine blades; a comparison between shell and 2D-solid models. *Wind. Eng.* **2005**, *29*, 25–31. [CrossRef]
8. Gabriel, E.T.; Mueller, T.J. Low-aspect-ratio wing aerodynamics at low Reynolds number. *AIAA J.* **2004**, *42*, 865–873.

9.   Ostowari, C.; Naik, D. Post stall studies of untwisted varying aspect ratio blades with an NACA 4415 airfoil section-Part I. *Wind. Eng.* **1984**, *9*, 176–194.
10.   Wizelius, T. *Developing Wind Power Projects: Theory and Practice*; Routledge: London, UK, 2015.
11.   Carpman, N. Turbulence Intensity in Complex Environments and Its Influence on Small Wind Turbines. Master's Thesis, Uppsala University, Uppsala, Sweden, 2011.
12.   Lubitz, W.D. Impact of ambient turbulence on performance of a small wind turbine. *Renew. Energy* **2014**, *61*, 69–73. [CrossRef]
13.   Fan, X.; Ge, M.; Tan, W.; Li, Q. Impacts of coexisting buildings and trees on the performance of rooftop wind turbines: An idealized numerical study. *Renew. Energy* **2021**, *177*, 164–180. [CrossRef]
14.   Bukala, J.; Damaziak, K.; Kroszczynski, K.; Krzeszowiec, M.; Malachowski, J. Investigation of parameters influencing the efficiency of small wind turbines. *J. Wind. Eng. Ind. Aerodyn.* **2015**, *146*, 29–38. [CrossRef]
15.   Probst, O.; Martínez, J.; Elizondo, J.; Monroy, O. Small wind turbine technology. *Wind Turbines*; 2011; pp. 107–136. Available online: https://www.intechopen.com/chapters/14799 (accessed on 9 April 2023).
16.   Kishore, R.A.; Coudron, T.; Priya, S. Small-scale wind energy portable turbine (SWEPT). *J. Wind. Eng. Ind. Aerodyn.* **2013**, *116*, 21–31. [CrossRef]
17.   Jain, P. *Wind Energy Engineering*; McGraw-Hill Education: New York, NY, USA, 2016.
18.   Burton, T.; Chichester, J. *Handbook of Wind Energy*; John Wiley & Sons: Hoboken, NJ, USA, 2001.
19.   Rahgozar, S.; Pourrajabian, A.; Kazmi, S.A.A.; Kazmi, S.M.R. Performance analysis of a small horizontal axis wind turbine under the use of linear/nonlinear distributions for the chord and twist angle. *Energy Sustain. Dev.* **2020**, *58*, 42–49. [CrossRef]
20.   Xudong, W.; Shen, W.Z.; Zhu, W.J.; Sørensen, J.N.; Jin, C. Shape optimization of wind turbine blades. *Wind. Energy: Int. J. Prog. Appl. Wind. Power Convers. Technol.* **2009**, *12*, 781–803. [CrossRef]
21.   Tenguria, N.; Mittal, N.D.; Ahmed, S. Investigation of blade performance of horizontal axis wind turbine based on blade element momentum theory (BEMT) using NACA airfoils. *Int. J. Eng. Sci. Technol.* **2010**, *2*, 64565. [CrossRef]
22.   Tahani, M.; Kavari, G.; Masdari, M.; Mirhosseini, M. Aerodynamic design of horizontal axis wind turbine with innovative local linearization of chord and twist distributions. *Energy* **2017**, *131*, 78–91. [CrossRef]
23.   Neto, J.X.V.; Junior, E.J.G.; Moreno, S.R.; Ayala, H.V.H.; Mariani, V.C.; dos Santos Coelho, L. Wind turbine blade geometry design based on multi-objective optimization using metaheuristics. *Energy* **2018**, *162*, 645–658. [CrossRef]
24.   Sriti, M. Improved blade element momentum theory (BEM) for predicting the aerodynamic performances of horizontal Axis wind turbine blade (HAWT). *Tech. Mech. Eur. J. Eng. Mech.* **2018**, *38*, 191–202.
25.   Lanzafame, R.A.; Messina, M. Fluid dynamics wind turbine design: Critical analysis, optimization and application of BEM theory. *Renew. Energy* **2007**, *32*, 2291–2305. [CrossRef]
26.   Moradtabrizi, H.; Nejat, A. Aerodynamic design and optimization of a megawatt wind turbine blade based on blade element momentum theory. *Modares Mech. Eng.* **2016**, *15*, 279–290.
27.   Bavanish, B.; Thyagarajan, K. Optimization of power coefficient on a horizontal axis wind turbine using bem theory. *Renew. Sustain. Energy Rev.* **2013**, *26*, 169–182. [CrossRef]
28.   Wang, Q.; Wang, J.; Chen, J.; Luo, S.; Sun, J. Aerodynamic shape optimized design for wind turbine blade using new airfoil series. *J. Mech. Sci. Technol.* **2015**, *29*, 2871–2882. [CrossRef]
29.   Tahani, M.; Maeda, T.; Babayan, N.; Mehrnia, S.; Shadmehri, M.; Li, Q.; Masdari, M. Investigating the effect of geometrical parameters of an optimized wind turbine blade in turbulent flow. *Energy Convers. Manag.* **2017**, *153*, 71–82. [CrossRef]
30.   Chaudhary, M.K.; Roy, A. Design & optimization of a small wind turbine blade for operation at low wind speed. *World J. Eng.* **2015**, *12*, 83–94.
31.   Tahani, M.; Kavari, G.; Mirhosseini, M.; Ghiyasi, S. Different functionalized chord and twist distributions in aerodynamic design of HAWTs. *Environ. Prog. Sustain. Energy* **2019**, *38*, 13108. [CrossRef]
32.   Pourrajabian, A.; Afshar, P.A.N.; Ahmadizadeh, M.; Wood, D. Aero-structural design and optimization of a small wind turbine blade. *Renew. Energy* **2016**, *87*, 837–848. [CrossRef]
33.   Pourrajabian, A. Effect of blade profile on the external/internal geometry of a small horizontal axis wind turbine solid/hollow blade. *Sustain. Energy Technol. Assess.* **2022**, *51*, 101918. [CrossRef]
34.   Abdelsalam, A.M.; El-Askary, W.A.; Kotb, M.A.; Sakr, I.M. Experimental study on small scale horizontal axis wind turbine of analytically-optimized blade with linearized chord twist angle profile. *Energy* **2021**, *216*, 119304. [CrossRef]
35.   Song, Q.; David Lubitz, W. Design and testing of a new small wind turbine blade. *J. Sol. Energy Eng.* **2014**, *136*, 034502. [CrossRef]
36.   Refan, M.; Hangan, H. Aerodynamic performance of a small horizontal axis wind turbine. *J. Sol. Energy Eng.* **2012**, *134*, 021013. [CrossRef]
37.   Suresh, A.; Rajakumar, S. Design of small horizontal axis wind turbine for low wind speed rural applications. *Mater. Today Proc.* **2020**, *23*, 16–22. [CrossRef]
38.   Mansi, A.; Aydin, D. The impact of trailing edge flap on the aerodynamic performance of small-scale horizontal axis wind turbine. *Energy Convers. Manag.* **2022**, *256*, 115396. [CrossRef]
39.   Masters, I.; Chapman, J.C.; Willis, M.R.; Orme, J.A.C. A robust blade element momentum theory model for tidal stream turbines including tip and hub loss corrections. *J. Mar. Eng. Technol.* **2011**, *10*, 25–35. [CrossRef]
40.   Liu, S.; Janajreh, I. Development and application of an improved blade element momentum method model on horizontal axis wind turbines. *Int. J. Energy Environ. Eng.* **2012**, *3*, 30. [CrossRef]

41. Ning, A.; Hayman, G.; Damiani, R.; Jonkman, J.M. Development and validation of a new blade element momentum skewed-wake model within AeroDyn. In Proceedings of the 33rd Wind Energy Symposium, Kissimmee, FL, USA, 5–9 January 2015; p. 0215.

42. Wood, D.H. Application of extended vortex theory for blade element analysis of horizontal-axis wind turbines. *Renew. Energy* **2018**, *121*, 188–194. [CrossRef]

43. Kabir, I.F.S.A.; Ng, E.Y.K. Insight into stall delay and computation of 3D sectional aerofoil characteristics of NREL phase VI wind turbine using inverse BEM and improvement in BEM analysis accounting for stall delay effect. *Energy* **2017**, *120*, 518–536. [CrossRef]

44. Wang, L.; Quant, R.; Kolios, A. Fluid structure interaction modelling of horizontal-axis wind turbine blades based on CFD and FEA. *J. Wind. Eng. Ind. Aerodyn.* **2016**, *158*, 11–25. [CrossRef]

45. Cai, X.; Gu, R.; Pan, P.; Zhu, J. Unsteady aerodynamics simulation of a full-scale horizontal axis wind turbine using CFD methodology. *Energy Convers. Manag.* **2016**, *112*, 146–156. [CrossRef]

46. Fu, P.; Farzaneh, M. A CFD approach for modeling the rime-ice accretion process on a horizontal-axis wind turbine. *J. Wind. Eng. Ind. Aerodyn.* **2010**, *98*, 181–188. [CrossRef]

47. Sayed, M.; Lutz, T.; Krämer, E.; Shayegan, S.; Ghantasala, A.; Wüchner, R.; Bletzinger, K.U. High fidelity CFD-CSD aeroelastic analysis of slender bladed horizontal-axis wind turbine. *J. Phys. Conf. Ser.* **2016**, *753*, 042009. [CrossRef]

48. Navinkumar, B.; Parammasivam, K.M.; Rajendran, S.; Mohanavel, V. CFD analysis of horizontal axis wind turbine braking system using chordwise spacing. *Mater. Today Proc.* **2021**, *37*, 542–552. [CrossRef]

49. Guo, T.; Lu, Z.; Tang, D.; Wang, T.; Dong, L. A CFD/CSD model for aeroelastic calculations of large-scale wind turbines. *Sci. China Technol. Sci.* **2013**, *56*, 205–211. [CrossRef]

50. Cai, X.; Pan, P.; Zhu, J.; Gu, R. The analysis of the aerodynamic character and structural response of large-scale wind turbine blades. *Energies* **2013**, *6*, 3134–3148. [CrossRef]

51. Hasan, M.M.; El-Shahat, A.; Rahman, M. Performance investigation of three combined airfoils bladed small scale horizontal axis wind turbine by BEM and CFD analysis. *J. Power Energy Eng.* **2017**, *5*, 1. [CrossRef]

52. Bugała, A.; Roszyk, O. Investigation of an innovative rotor modification for a small-scale horizontal axis wind turbine. *Energies* **2020**, *13*, 2649. [CrossRef]

53. Yossri, W.; Ayed, S.B.; Abdelkefi, A. Airfoil type and blade size effects on the aerodynamic performance of small-scale wind turbines: Computational fluid dynamics investigation. *Energy* **2021**, *229*, 120739. [CrossRef]

54. Jackson, R.S.; Amano, R. Experimental study and simulation of a small-scale horizontal-Axis wind turbine. *J. Energy Resour. Technol.* **2017**, *139*, 4036051. [CrossRef]

55. Kishore, R.A.; Priya, S. Design and experimental verification of a high efficiency small wind energy portable turbine (SWEPT). *J. Wind. Eng. Ind. Aerodyn.* **2013**, *118*, 12–19. [CrossRef]

56. Aftab, S.M.A.; Mohd Rafie, A.S.; Razak, N.A.; Ahmad, K.A. Turbulence model selection for low Reynolds number flows. *PLoS ONE* **2016**, *11*, e0153755. [CrossRef]

57. Saad, Y.; Schultz, M.H. GMRES: A generalized minimal residual algorithm for solving nonsymmetric linear systems. *SIAM J. Sci. Stat. Comput.* **1986**, *7*, 856–869. [CrossRef]

58. Nemes, A.; Sherry, M.; Jacono, D.L.; Blackburn, H.M.; Sheridan, J. Evolution and breakdown of helical vortex wakes behind a wind turbine. *J. Phys. Conf. Ser.* **2014**, *555*, 012077. [CrossRef]

59. Li, D.; Ho, S.C.M.; Song, G.; Ren, L.; Li, H. A review of damage detection methods for wind turbine blades. *Smart Mater. Struct.* **2015**, *24*, 033001. [CrossRef]

60. Chateauminois, A.; Chabert, B.; Soulier, J.P.; Vincent, L. Hygrothermal ageing effects on the static fatigue of glass/epoxy composites. *Composites* **1993**, *24*, 547–555. [CrossRef]

61. Wood, D. Introduction to Wind Turbine Technology. In *Small Wind Turbines*; Springer: London, UK, 2011; pp. 1–29.